JOURNAL OF COMPUTATIONAL PHYSICS 107, 188–198 (1993)

Smoothed Particle Hydrodynamics Applied to Relativistic Spherical Collapse

PATRICK J. MANN

Department of Applied Mathematics, University of Western Ontario, London, Ontario, Canada N6A 3K7

Received April 24, 1991; revised October 11, 1992

The *smoothed particle hydrodynamics* method was applied in a previous paper to a relativistic shock tube test problem. In this paper the method is further extended to relativistic, self-gravitating spherical collapse and compared directly with an equivalent finite element method code. The particle code uses smoothed particle hydrodynamics for the fluid and approximates the gravitational potentials with finite elements. The finite element code uses a similar potential solver, but it evolves fluid quantities with finite elements. The direct particle method was unstable at the centre, the surface, and during the formation of horizons, but a Galerkin weighted residual technique successfully solved all these instabilities. In direct comparison with finite elements smoothed particle hydrodynamics produced results which were generally smoother (for the same number of particles and nodes) but otherwise in good agreement. The smoothed particle hydrodynamics method was certainly able to model this self-gravitating fluid.

1. INTRODUCTION

The smoothed particle hydrodynamics method (SPH) of Lucy, Gingold, and Monaghan [9, 13] has become a widely used method in the study of self-gravitating fluid bodies. Monaghan and Lahy suggested an extension to relativity in [14], and I used this method, together with a further extension to model a one-dimensional shock tube [10]. That shock problem did not include gravity, but it did show that SPH was a viable method for fluids in special relativity. The next stage was clearly to include gravity. This paper will report on my first tests with SPH for a self-gravitating, relativistic fluid.

I have chosen to model a spherically symmetry relativistic fluid. My approach is to approximate the fluid with SPH, but to model the gravitational potentials with a finite element method (FEM). Einstein's theory is a geometric theory so the particle–particle forces of Newton's theory (and classical SPH) cannot be used. It may be possible to use SPH to approximate the gravitational terms, but in relativity the metric can evolve dynamically even in the absence of matter. Therefore the fluid particles would have to be augmented with gravitational "particles" moving along their own geodesics. I have not done this.

Grid-based potential solvers have also been used in Newtonian SPH (see [15], for instance), but most codes now use the specifically particle–particle tree algorithms. Unfortunately these powerful techniques cannot be applied in relativity. The Newtonian potential solver of [15] uses finite difference methods. I have preferred the FEM because the FEM interpolation can be used to interpolate back to the particles in a consistent manner.

The particle-in-cell method has been used by [4], but this method does not include the underlying "no grid" basis of SPH.

An SPH approximation can be viewed in two ways: as a set of numerical interpolations of the functions defining a physical model and as a specific physical model using "particles" of fluid. The second approach is that of classic SPH and requires the use of particles which possess physical properties. For instance, [8] uses specifically covariant particles.

I have preferred to use the first approach. In this case the physical quantity is the interpolation, and not the interpolation basis (the particles). Therefore I can write the relativistic fluid equations directly as differential equations and apply SPH as a method of discretizing these equations. This ensures that the metric and coordinate choices required in numerical relativity do not appear explicitly in the particle (interpolation basis) choice.

This SPH method is similar to a finite element approach in which the elements can now overlap and are defined only by a size and a position. The fundamental SPH advantages of freely moving particles with no grid are preserved.

I will first write the equations for relativistic collapse and then introduce the approximations which are to be used by SPH and FEM. Next the finite element solution for the gravitational potentials will be outlined, and then a more detailed exposition of the SPH discretization of the fluid equations will be made. Unfortunately early tests showed

0021-9991/93 $5.00

that the discretization which I used in [10] was not able to handle the coordinate singularity at the centre, and it also showed instabilities near the surface. Therefore a significant modification is made by introducing a weighted residual SPH method. This new method is first tested with the relativistic shock tube and some results presented.

Further tests use the complete code with various choices of initial conditions and are compared directly with a FEM code. There are three general scenarios: static evolution, complete collapse, and collapse-and-bounce. Some typical runs from each of these are presented and discussed.

The conventions of Misner, Thorne, and Wheeler [12] are used in this paper, and the units take the gravitational constant G and the speed of light c to be one.

2. THE EQUATIONS

The metric is the radial gauge, polar sliced version,

$$ds^2 = -B^2(1-2m/r)\,dt^2 + (1-2m/r)^{-1}\,dr^2 + r^2(d\theta^2 + \sin^2\theta\,d\phi^2) \tag{1}$$

where r is the Schwarzschild radial coordinate. The quantities m and B are functions of r and t. Note that $\sqrt{-g} = r^2 \sin\theta B$.

The energy-momentum tensor is given by $T^\beta_\alpha = (p+\rho)\,u_\alpha u^\beta + p g^\beta_\alpha$, where p is the pressure, ρ is the total energy density, and u^α is the fluid four-velocity. For convenience define ρ_0 to be the rest energy, e to be the internal (thermal) energy, and w to be the relativistic enthalpy. Then

$$\rho = \rho_0 + e \tag{2}$$

and

$$w = (p+\rho)/\rho_0. \tag{3}$$

The equation of state is assumed to be polytropic,

$$p = (\gamma - 1)e \tag{4}$$

which gives

$$w = 1 + \gamma\varepsilon, \tag{5}$$

where $\varepsilon = e/\rho_0$ is the specific internal energy.

The fluid four-velocity u^α is the vector $(u^t, u^r, 0, 0)$ due to the symmetry, and for convenience define the three-velocity $V = u^r/u^t$.

Conservation of rest mass $(\rho_0 u^\alpha)_{;\alpha} = 0$ then gives the equation

$$D_{,t} + \frac{1}{r^2}(r^2 VD)_{,r} = 0, \tag{6}$$

where $D = Bu^t\rho_0$. The quantity $Bu^t = \sqrt{-g}\,u^t/(r^2\sin\theta)$ appears regularly so define

$$A = Bu^t, \tag{7}$$

in which case

$$D = A\rho_0. \tag{8}$$

The fluid equations are derived from $T^\beta_{\alpha;\beta} = 0$ with the result that

$$r^2 S_{,t} + (r^2 VS)_{,r} = -r^2 B p_{,r} - wDA\left(r^2 B_{,r}(1-2m/r) + B\left(\frac{w^2 + 2Z^2(1-2m/r)}{w^2 + Z^2(1-2m/r)}\right)(m - rm_{,r})\right) \tag{9}$$

and

$$r^2 E_{,t} + (r^2 VE)_{,r} = -p(r^2 A_{,t} + (r^2 VA)_{,r}), \tag{10}$$

where

$$S = wDu_r = T^t_r \tag{11}$$

$$E = Ae \tag{12}$$

and

$$Z = S/D. \tag{13}$$

Combining these quantities and using the velocity normalization $u^\alpha u_\alpha = -1$ gives

$$V = ZB((1-2m/r)(w^2 + Z^2(1-2m/r)))^{-1/2} \tag{14}$$

$$A = B\left(\frac{1-2m/r}{B^2(1-2m/r)^2 - V^2}\right)^{1/2} \tag{15}$$

and

$$\varepsilon = E/D. \tag{16}$$

Einstein's equations are particularly simple in this coordinate system:

$$m_{,r} = 4\pi r^2\left(\frac{1-2m/r}{w^2 + Z^2(1-2m/r)}\right)^{1/2} \times (w(D+E) + DZ^2(1-2m/r)) \tag{17}$$

$$\frac{B_{,r}}{B} = 4\pi r D((1-2m/r)(w^2 + Z^2(1-2m/r)))^{-1/2} \times (w^2 + 2Z^2(1-2m/r)). \tag{18}$$

There are time-dependent versions of these equations but only the above two are required (consistency is guaranteed by the Bianchi identities). In spherical symmetry these constraint equations are particularly simple, and there is no necessity for the use of the evolution equations.

The boundary conditions are:

$$\begin{aligned} &\text{Centre:} \quad r=0,\ m=0,\ m_{,r}=0,\ B_{,r}=0,\ S=0,\ V=0 \\ &\text{Surface:} \quad B=1,\ \rho_0=0,\ e=0. \end{aligned} \tag{19}$$

The Einstein equations (17) and (18) can be inserted in Eq. (9) to derive

$$r^2 S_{,t}+(r^2 VS)_{,r}=-B\left(r^2 p_{,r}+\frac{D}{\sqrt{1-2m/r}} \times\left(\frac{w^2D^2+2S^2(1-2m/r)}{\sqrt{w^2D^2+S^2(1-2m/r)}}\right)(m+4\pi r^3 p)\right). \tag{20}$$

3. THE APPROXIMATIONS

Useful descriptions of classic SPH can be found in [5 or 7], and details of the extension to relativity can be found in [10, 14]. The relativistic "density" D is analogous to the Newtonian density so the SPH approximation is written

$$D(r,t)\cong\sum_{j=1}^{n} m_j(t)\,W(r-r_j(t),h_j(t)), \tag{21}$$

where $m_j(t)$ is the mass of "particle" j (equivalent to the rest density ρ_0 integrated over a suitable volume of the three-slice) and $r_j(t)$ is the position of the particle. There are n particles.

The kernel or smoothing function $W(x,h)$ gives the shape of the particle as a function of position x and size h. Generally W is assumed to be symmetric around $x=0$, but the smoothing length h_j is allowed to vary from particle to particle and is also a function of time.

However, there is a symmetry in this problem and therefore some thought has to be given to the specific choice. Let $W_{ml}(x,h)$ be the standard cubic spline kernel of Monaghan and Lattanzio [15]:

$$W_{ml}(x,h)=\frac{1}{h}\begin{cases}1-(3/2)\,|x/h|^2+(3/4)\,|x/h|^3, & 0<|x/h|\leqslant 1\\ (1/4)(2-|x/h|)^3, & 1<|x/h|\leqslant 2\\ 0, & \text{otherwise.}\end{cases} \tag{22}$$

A first attempt took $W(x,h)=W_{ml}(x,h)$ and then included a reflection at the centre, but this invariably resulted in large oscillations in the density approximation at the centre. A far better approximation can be obtained by writing antisymmetric and symmetric combinations respectively:

$$\begin{aligned} W^{(a)}(r-r_i,h_i)&=W_{ml}(r-r_i,h_i)-W_{ml}(-r-r_i,h_i)\\ W^{(s)}(r-r_i,h_i)&=W_{ml}(r-r_i,h_i)+W_{ml}(-r-r_i,h_i). \end{aligned} \tag{23}$$

This ensures that symmetric functions such as the density will be smooth at the centre, and antisymmetric functions such as the momentum will vanish at the centre. Note that the symmetrization is effective only within $2h$ of the centre. Farther out, both kernels are identical to W_{ml}.

These combinations are normalized to ensure that

$$\int_0^{\text{surface}} 4\pi r^2 W^{(a)}(r-r_i,h_i)\,dr=1 \tag{24}$$

and similarly for $W^{(s)}$. For particles within $2h$ of the centre there is a position-dependent contribution because the integral stops at $r=0$, but this is straightforward to include.

For convenience define the short forms:

$$\begin{aligned} W_i^{(a)}(r)&\equiv W^{(a)}(r-r_i,h_i)\\ W_i^{(s)}(r)&\equiv W^{(s)}(r-r_i,h_i). \end{aligned} \tag{25}$$

Various time derivatives of $W_i^{(a)}$ and $W_i^{(s)}$ will be necessary in the following discussion. These always include the requisite contributions from $h_i(t)$ and $r_i(t)$ ensuring that any choice of position and smoothing length is allowed.

The symmetric quantity D is then approximated by

$$D(r,t)\cong\sum_{j=1}^{n} m_j(t)\,W_j^{(s)}(r). \tag{26}$$

The symmetric quantity E can be approximated by the mass-weighted approximation

$$E(r,t)\cong\sum_{j=1}^{n} m_j(t)\,\varepsilon_j(t)\,W_j^{(s)}(r) \tag{27}$$

and the antisymmetric quantity S by

$$S(r,t)\cong\sum_{j=1}^{n} m_j(t)\,Z_j(t)\,W_j^{(a)}(r), \tag{28}$$

where $\varepsilon_j(t)$ and $Z_j(t)$ are expansion coefficients which will be computed during the evolution.

As mentioned in the Introduction these are not standard SPH expressions, and the kernel is not covariant. The coefficients m_i, Z_i, and ε_i define the interpolation and will be evolved, but only the complete interpolations D, S, and E are used in the differential equations. Note, for instance, that $\varepsilon_i\neq E(r_i)/D(r_i)$, in general.

The following definitions will be useful in the derivation of the SPH evolution equations:

$$D_i \equiv D(r_i), \qquad E_i \equiv E(r_i), \qquad S_i \equiv S(r_i). \tag{29}$$

The two metric quantities m and B are approximated on a finite element mesh with cubic Hermite splines:

$$m(r, t) = \sum_j (m_{1j} N_{1j}(r) + m_{2j} N_{2j}(r)) \tag{30}$$

and similarly for B. The shape functions $N_{i1}(r)$ and $N_{2i}(r)$ are chosen to ensure that

$$m(r_i^{(g)}, t) = m_{1i} \qquad \text{and} \qquad \left(\frac{\partial m(r, t)}{\partial r}\right)_{r = r_i^{(g)}} = m_{2i}, \tag{31}$$

where $r_j^{(g)}$ are the positions of the grid nodes. Equations (17) and (18) are constraint equations, so in this spherically symmetric case the mesh can be defined independently on each time slice and there is no need for explicit time dependencies.

This completes the description of the approximations. All other quantities can be derived from D, S, E, m, and B with the help of the definitions in Section 2. Interpolations between grid and particle are performed by evaluating the SPH approximations (26), (27), and (28) at grid positions and evaluating the FEM approximation (30) at particle positions. In particular, it is convenient to define

$$V_i \equiv V(r_i), \qquad p_i \equiv p(r_i) \tag{32}$$

from Eqs. (14) and (4).

4. THE FEM CONSTRAINT SOLVER

The two Einstein equations (17) and (18) are discretized by a two-point weighted residual method and then solved from the centre outwards (see [11] for details). The two equations require Z, D, and E on the grid. The quantities S, D, and E are computed directly from the SPH interpolation and then $Z = S/D$ is immediately calculated on the grid nodes. Linear interpolations of Z, D, and E are then used by the FEM solver.

I have tested more explicit (and slower) methods in which Z is computed directly in the FEM discretization, but there is no significant difference in the results.

5. THE SPH TIME EVOLUTION

In [10] I tested a simple time discretization (for a 1D Shock tube) which inserted the SPH approximations directly into the evolution equations (6), (9), (10) and collocated them at particle positions. For the spherically symmetric case this results in $1/D$ and $1/r$ terms which become singular at the surface and centre. A careful choice of particle positions ensures that these terms stay finite, but even in a simple Newtonian test case the centre and surface approximations become unstable. The same behaviour occurs when other coordinate singularities (i.e., $1 - 2m/r \to 0$) appear, so a better method is required. Similar problems occur with FEM simulations, and they are solved by using a weighted residual method with a factor $r^2 D$ included in the weight. The same approach can be taken here.

Benz [2] has derived the standard SPH from a weighted residual approach which used Galerkin weights. This nice method resulted in a more consistent version of the energy equation which solved some numerical problems concerned with negative internal energies. However, he did not include different weights.

First write the typical equation (9) in the form

$$r^2 S_{,t} = -(r^2 V S)_{,r} - g. \tag{33}$$

Now apply the weighted residual method,

$$\int (r^2 S_{,t})\, W_i^{(s)}(r)\, dr = -\int (g + (r^2 V S)_{,r})\, W_i^{(s)}(r)\, dr, \tag{34}$$

where all quantities are now the SPH or FEM approximations as necessary.

To preclude any artificial vanishing of the weights I have used the symmetric kernel as the weight function everywhere.

These expressions are, in general, not analytically integrable, so a numerical quadrature must be used. An obvious choice is to use quadrature points at the particle positions r_j,

$$\sum_{j=1}^{n} (r_j^2 S_{,t}(r_j))\, W_{ij}^{(s)} = -\sum_{j=1}^{n} (g_j + \nabla_j (r^2 V S))\, W_{ij}^{(s)}, \tag{35}$$

where $g_j = g(r_j)$, $W_{ij}^{(s)} \equiv W^{(s)}(r_j - r_i, h_i)$, and ∇_j is the partial derivative with respect to r evaluated at r_j.

The left side of (35) can be expanded to give

$$\begin{aligned} &\sum_{k=1}^{n} \left(\frac{dZ_k}{dt} m_k W_{kj}^{(a)} \sum_{j=1}^{n} r_j^2 W_{ij}^{(s)}\right) \\ &\quad = -\sum_{j=1}^{n} r_j^2 W_{ij}^{(s)} \left(\sum_{k=1}^{n} Z_k \left(\frac{dm_k}{dt} W_{kj}^{(a)} + m_k \dot{W}_{kj}^{(a)}\right)\right) \\ &\qquad - \sum_{j=1}^{n} (g_j + \nabla_j (r^2 V S))\, W_{ij}^{(s)}, \end{aligned} \tag{36}$$

where

$$\dot{W}_{ij}^{(a)} \equiv \partial W_i^{(a)}/\partial t \tag{37}$$

evaluated at $r = r_j$ (and similarly for $\dot{W}_{ij}^{(s)}$). These derivatives include the particle velocity $r_{i,t}$ and the smoothing length variation $h_{i,t}$.

Note that Z_k and m_k are functions of t only. If the particle velocity is the fluid velocity then the derivative is indeed a Lagrangian derivative, but this will not be true in general.

The left side of this equation is a matrix expression of the form $\mathbf{A}\, d\mathbf{z}/dt$, where $\mathbf{z}$ is the vector of Z_k. The matrix $\mathbf{A}$ is sparse because $W_{ij}^{(s)}$ is localized, but its structure is variable as particles overlap during the evolution. To avoid any matrix solvers I have applied the FEM technique of condensation or mass-lumping ([1], for instance) and approximate:

$$\sum_{k=1}^{n} \left(\frac{dZ_k}{dt} m_k \sum_{j=1}^{n} r_j^2 W_{ij}^{(s)} W_{kj}^{(a)} \right) \cong \frac{dZ_i}{dt} \sum_{j=1}^{n} r_j^2 W_{ij}^{(s)} \sum_{k=1}^{n} m_k W_{kj}^{(a)}. \tag{38}$$

Define

$$L_i^{(a)} \equiv \sum_{j=1}^{n} r_j^2 W_{ij}^{(s)} \sum_{k=1}^{n} m_k W_{kj}^{(a)}. \tag{39}$$

Then from (35) and (36)

$$\frac{d}{dt} Z_i = \mathscr{Z}_i, \tag{40}$$

where

$$\mathscr{Z}_i = -\left(\sum_{j=1}^{n} r_j^2 W_{ij}^{(s)} \left(\sum_{k=1}^{n} Z_k \left(\frac{dm_k}{dt} W_{kj}^{(a)} + m_k \dot{W}_j^{(a)} \right) \right) + \sum_{j=1}^{n} (g_j + \nabla_j (r^2 VS))\, W_{ij}^{(s)} \right) \Big/ L_i^{(a)} \tag{41}$$

which is an evolution equation for Z_i.

Similarly, the mass conservation equation (6) can be discretized with a weighted residual method to produce:

$$\frac{d}{dt} m_i = \mathscr{M}_i, \tag{42}$$

where

$$\mathscr{M}_i = -\left(\sum_{j=1}^{n} r_j^2 W_{ij}^{(s)} \sum_{k=1}^{n} m_k \dot{W}_{kj}^{(s)} + \sum_{j=1}^{n} \nabla_j (r^2 VD)\, W_{ij}^{(s)} \right) \Big/ L_i^{(s)} \tag{43}$$

and

$$L_i^{(s)} \equiv \sum_{j=1}^{n} r_j^2 W_{ij}^{(s)} \sum_{k=1}^{n} m_k W_{kj}^{(s)}. \tag{44}$$

Unfortunately Eq. (10) for E includes a time derivative of A on the right side. The quantity A can show extremely nonlinear behaviour (horizons, where $1 - 2m/r \to 0$), so various specialized forms of A have been used (see [3 or 6], for instance). I will be using a predictor–corrector evolution, where A can be approximated with the most up-to-date information available, so I have decided to use a simple scheme with

$$\left(\frac{DA}{dt} \right)_i^t \equiv \frac{A_i^t - A_i^{t-1}}{\Delta t}, \tag{45}$$

where D/dt is the derivative along the particle track and the superscript indicates the time slice (from time t^{t-1} to time t^t).

Then the right side of (10) evaluated at a particle position can be written as

$$\mathscr{F}_k \left(\frac{DA}{dt} \right)_k^t + \mathscr{G}_k, \tag{46}$$

where $\mathscr{F}_k \equiv -p_k r_k^2$ and

$$\mathscr{G}_k \equiv -p_k \left(r_k^2 V_k \left(r_k - \frac{dr_k}{dt} \right) \nabla_k A + r_k^2 A_k \nabla_k V + 2 r_k V_k A_k \right). \tag{47}$$

The weighted residual method applied as for Z then gives

$$\frac{d\varepsilon_i}{dt} = \mathscr{E}_i + \left(\sum_{j=1}^{n} \mathscr{G}_j \left(\frac{DA}{dt} \right)_j^t W_{ij}^{(s)} \right) \Big/ L_i^{(s)}, \tag{48}$$

where

$$\mathscr{E}_i = -\left(\sum_{j=1}^{n} r_j^2 W_{ij}^{(s)} \left(\sum_{k=1}^{n} \varepsilon_k (m_{k,t} W_{kj}^{(s)} + m_k \dot{W}_{kj}^{(s)}) \right) + \sum_{j=1}^{n} \mathscr{G}_j W_{ij}^{(s)} \right) \Big/ L_i^{(s)}. \tag{49}$$

There are two remaining evolution equations: for r_i and h_i. For this first attempt I have chosen the simple Lagrangian version for particle positions:

$$\frac{dr_i}{dt} = V_i. \tag{50}$$

The smoothing length should be chosen to keep a constant number of particles within range of any given particle. There are a number of possible variations (see [2]), most of which perform well with, for instance, shock tube tests (Newtonian and relativistic) and other Newtonian simulations. I have found that these standard techniques produce unstable oscillations when shocks move out towards the surface of some of my spherical simulations. A smooth evolution is required, with a scale approximately equal to a smoothing length. The following formula has proven to be extremely robust:

$$\frac{1}{h_i}\frac{dh_i}{dt} = \alpha_h \frac{1}{D_i} \sum_{j=1}^{n} m_j \nabla_j V W_{ij}^{(s)}. \tag{51}$$

This is an approximation to

$$\frac{1}{h}\frac{dh}{dt} \propto -\frac{1}{D}\frac{dD}{dt}. \tag{52}$$

A value of $\frac{1}{2}$ for the proportionality constant α_h seems to be sufficient. Values closer to one can in practice lead to very small h where only one or two particles overlap.

6. ARTIFICIAL VISCOSITY

I have included a simple artificial viscosity to smooth shocks. I experimented with the Baker smoothing technique [1] introduced in [10], but unfortunately this method was never able to smooth shocks which approached the surface. Such shocks amplify as they move into the low density regions near the surface, and the Baker smoothing was insufficient to stop a runaway oscillation at the surface. This is unfortunate as the Baker smoothing gave significantly flatter and sharper results with the shock tube tests.

It is possible to use an artificial viscosity near the surface and Baker smoothing in the body of the "star." However, this method was not robust, as model-dependent fine tuning of the position and type of the crossover was required.

Therefore a standard artificial viscosity (see [5, 7], for instance) has been incorporated as follows:

Replace p in $T_{\alpha\beta}$ with $p + q$, where

$$q(r, t) = \sum_{j=1}^{n} m_j(t)\, \tilde{q}_j W_j^{(s)}(r) \tag{53}$$

$$\tilde{q}_j = \begin{cases} K_{q1} c_s(r_j)\, Q_j + K_{q2} Q_j^2, & \text{if } \nabla_j V < 0 \\ 0, & \text{otherwise} \end{cases} \tag{54}$$

and

$$Q_j = (1 + \varepsilon(r_j))\, h_j\, |\nabla_j V|; \tag{55}$$

c_s is the sound speed. The magnitude of the artificial viscosity is controlled by the parameters K_{q1} and K_{q2}. A suitable value for both these parameters is one.

7. A COMPLETE EVOLUTION STEP

A typical constraint sweep starts with particle quantities Z_i, ε_i, and m_i and proceeds as follows:

- Set up a grid.
- Calculate D, E, and S on the grid with the SPH approximation.
- Calculate Z on the grid from Eq. (13).
- Compute m_{1i}, m_{2i}, B_{1i}, and B_{2i} from the FEM discretization.
- Calculate m and B at the particle positions with the FEM approximation.

The evolution is a second-order predictor–corrector:

1. *Predict.*

(a) First-order evolution to next time step:

$$r_i^t = r_i^{t-1} + \Delta t\, V_i^{t-1}$$

$$m_i^t = m_i^{t-1} + \Delta t\, \mathscr{M}_i^{t-1}$$

$$Z_i^t = Z_i^{t-1} + \Delta t\, \mathscr{Z}_i^{t-1}$$

$$\varepsilon_i^t = \varepsilon_i^{t-1} + \Delta t\, \mathscr{E}_i^{t-1} + \Delta t \sum_{j=1}^{n} (\mathscr{F} W_{ij}^{(s)}/L_i^{(s)})^{t-1} \left(\frac{DA}{dt}\right)_j^t.$$

(b) A constraint sweep with the predicted values on the new time slice.

2. *Correct.*

(a) Calculate S, D, and E at particle positions.

(b) Calculate Z, V, and A from (13), (14), and (15).

(c) Evolve r_i from the centred difference version of Eq. (50) and evolve h_i from the centred difference version of Eq. (51).

(d) Calculate $\mathscr{M}_i^t$ from (46) and evolve m:

$$m_i^t = m_i^{t-1} + \tfrac{1}{2}\Delta t(\mathscr{M}_i^{t-1} + \mathscr{M}_i^t).$$

(e) Calculate $\mathscr{Z}_i^t$ and $\mathscr{E}_i^t$ from (51), (44) and evolve Z and E:

$$Z_i^t = Z_i^{t-1} + \tfrac{1}{2}\Delta t(\mathscr{Z}_i^{t-1} + \mathscr{Z}_i^t)$$

$$\varepsilon_i^t = \varepsilon_i^{t-1} + \tfrac{1}{2}\Delta t(\mathscr{E}_i^{t-1} + \mathscr{E}_i^t) + \Delta t \left(\sum_{j=1}^{n} \mathscr{F}_j^t \left(\frac{DA}{dt}\right)_j^t (W_{ij}^{(s)})^t \right) \Big/ L_i^{(s)}.$$

(f) A constraint sweep with the corrected values on the new time slice.

(g) Calculate V and A from (14) and (15) and evolve r_i and h_i again (see step (c)).

Some observations are in order at this point. m_i is separately evolved before Z_i and ε_i because such a scheme gives much better results in a shock tube test. Step 2(g) is required to ensure that an up-to-date value for A is always available for the ε evolution. Simple geodesic motion tests show this to be a necessary part of the predictor–corrector scheme.

The ε evolution includes DA/dt as a centred second-order approximation, but note that the multiplier $\mathscr{F}_j^i$ is not averaged in this implementation because its value on the previous time slice is not stored.

8. INITIAL DATA

The variables m, B, ρ_0, and ε are given initially on the nodes of a finite element grid, with the velocity assumed to be zero (a stationary initial configuration). Particle positions are then given. In this paper the particles are always evenly spaced.

The smoothing length is then calculated as a multiple of the interparticle spacing. Experiments with the shock tube [10] showed that a multiple of two was generally required. Smaller h resulted in poor approximations to the fluid forces between particles.

Next m_i is chosen to reflect the given density on the grid. I use a Newton-type iteration,

$$m_i^{(\text{new})} = m_i^{(\text{old})} + \eta({}^{(g)}D(r_i) - {}^{(s)}D(r_i))/W_{ii}^{(s)}, \qquad (56)$$

where ${}^{(g)}D(r_i)$ is the density variable D at particle positions computed from the finite element approximation and ${}^{(s)}D$ is the equivalent SPH approximation computed using the previous estimate of m_i. I have included a relaxation parameter $\eta = 0.5$ which ensures convergence.

This scheme converges quickly for particles within about $2h$ of the surface. Near the surface the SPH density reflects the shape of the kernel due to a paucity of particles and therefore cannot approximate the given density accurately.

A similar iteration is required to give ε_i, resulting in a complete data set on the particles. The evolution interpolates from the particles onto the grid used by the constraint solver so no initial data is required on the grid. Note that there is also no requirement that the input data be on the same grid as the constraint solver. I usually use some large number of nodes on the input grid (~ 500) to ensure accuracy in the initial model.

9. THE SHOCK TUBE TEST

The Riemann shock tube (non-gravitating) is a good first test for SPH. Sod's standard Newtonian version [17] has been extensively used by both SPH (see [5 or 7], for instance) and FEM (see [1]), but the relativistic case has been principally modelled with finite difference methods (see [3, 6]). I reported on an extensive set of tests with SPH in [10], but the methods used did not include the weighted residual integration. However, the weighted residual method has given very similar results. The analytic solution has been derived in [18].

Figure 1 is an illustration of a typical shock tube run. The fluid in the tube is polytropic with $\gamma = 2$, and has the initial conditions:

	Left side	Right side	
Density ρ	8.0	2.0	
Internal energy ε	1.0	0.0	
Smoothing length h	2.3×10^{-3}	Same	(57)
Mass per particle m_i	9.4×10^{-3}	2.3×10^{-3}	
Boundaries	-0.3	0.3	
Number of particles	256	256	

Note that the particles are evenly spaced with a variable mass which models the initial density. Evolution proceeds to a time $t = 0.25$. The artificial viscosity parameters are $K_{q1} = 1$ and $K_{q2} = 1$.

Generally the fit is good, with rest mass conserved to

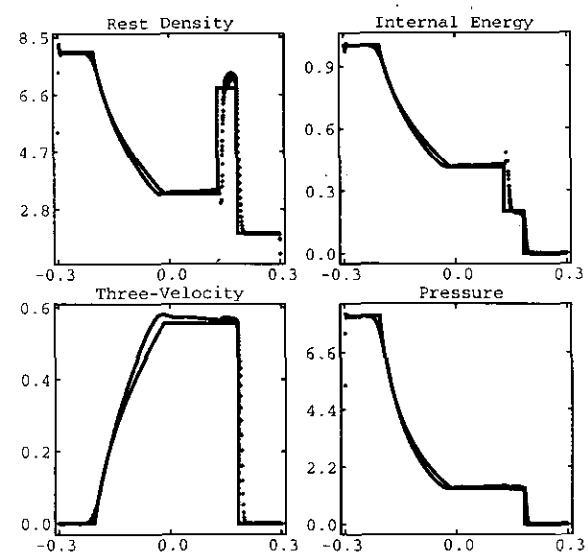

FIG. 1. The relativistic shock tube with conditions given in (57). The density ρ_0, three-velocity V, specific internal energy ε, and pressure p are plotted.

0.3%. The velocity plateau is overestimated, which is characteristic of all my tests, and this results in a small displacement of the contact discontinuity. The internal energy shows a slight spike on the contact discontinuity, which is also characteristic of these particle methods. The shock is rather smooth, but decreasing the artificial viscosity results in post-shock oscillations.

10. FURTHER TESTS

The complete code can be tested on static configurations, on pressureless collapse, and by comparing to a different code. I have constructed a separate FEM code to perform the comparison. This code approximates D, ε, and Z (not E and S) on a spatial FEM grid with linear splines, and then it evolves the nodal values with a second-order predictor–corrector similar to the one used for SPH. The constraint solver is identical to the SPH/FEM constraint solver except that ε and Z are used as basic variables. Smoothing is accomplished by including an artificial viscosity similar to Eq. (53).

The first tests of the complete code used as initial data a FEM solution of the Tolman–Oppenheimer–Volkov (TOV) equations describing static, spherical configurations. In these models I have taken $p=\rho_0^\gamma$, and have parameterized the models by the central enthalpy.

In the following discussion various time scales are used. The times given on the graphs are normalized as follows: Coordinate time is normalized by the coordinate time required for a test particle initially at the surface radius to fall half the distance to the event horizon in a Schwarzschild background (mass equals the mass of the initial configuration). Proper time at the surface is normalized by the proper time required by the test particle to reach the event horizon. Proper time at the centre is normalized by the proper time required for a pressureless (freefall) collapse to reach infinite central density.

Both the SPH and FEM can evolve initially stable models quite satisfactorily. Unstable models drift slowly away from equilibrium as numerical errors build up. Figure 2 illustrates a typical run with data:

$$\left.\begin{array}{l} w(\text{centre})=1.35 \\ \\ \gamma=5/3 \end{array}\right\} \begin{array}{l} \text{SPH: number of nodes} = 64, \\ \qquad \text{number of particles} = 128 \\ \text{FEM: number of nodes} = 64. \end{array} \tag{58}$$

This is a *marginally* stable polytrope, and, indeed, the model shows a slow evolution away from the initial model. The FEM model slowly contracts, with an increase in the central rest density of about 4% after 15 freefall times (proper time to infinite density at the centre). The SPH model expands with an equivalent 4% decrease in the central rest density. Surface position is slightly better, with the SPH model expanding by 3% and the FEM model decreasing by 1%. Metric mass m is nicely conserved (Fig. 2), and the change in the total particle mass (rest mass) is about the same.

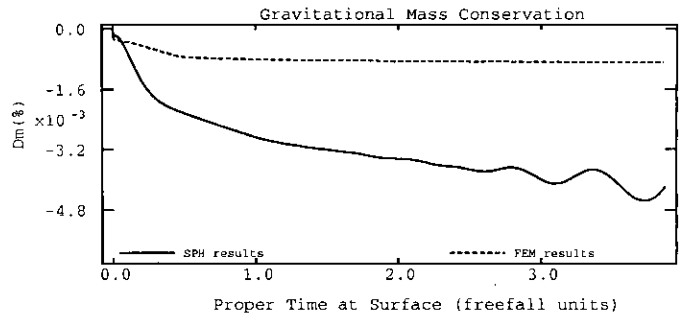

FIG. 2. Conservation of metric mass $m(r)$ at the surface for the static conditions given in (58).

This configuration should be stable, but clearly both SPH and FEM have pushed the marginally stable model over into an unstable regime, although it is interesting to note that SPH forces an expansion, while FEM forces a collapse.

Higher resolution improves the SPH runs. With 256 particles (64 grid nodes) the SPH simulation is more stable with a surface expansion of about 0.8%. However, the metric mass conservation is about the same. This suggests that the FEM grid (the same mesh size in both runs) is giving most of the error in metric mass conservation, and, indeed, the particle rest mass is better conserved than the metric mass.

The pressureless collapse of a homogeneous sphere has an analytic solution given by the Oppenheimer–Snyder metric [12]. An explicit transformation to polar slicing is also available [16], so a comparison to the analytic solution can be made.

This is a very difficult evolution for SPH because the singular behaviour in the density appears at the surface. However, except for a smooth tail at the surface, SPH gives excellent results. A typical evolution used 256 particles and 64 grid nodes and evolved until the central value of B (the lapse function) had decreased to about 0.5% of its initial value (in the units of [16], about $t=50$ M). At this point m and B were approximated to within 2% of the analytic solution.

The density clearly showed the SPH smoothing with the surface density spike turning over within $2h$ of the surface. At this point the density had reached approximately 50% of the maximum surface value in the analytic solution.

A more realistic pressureless collapse can be modelled by taking an initially static configuration and artifically setting $\varepsilon=0$ ($p=0$). The constraint equations for m and B must be solved again to obtain a consistent data set, but this can be done rather simply by using the FEM constraint solver on the initial data grid.

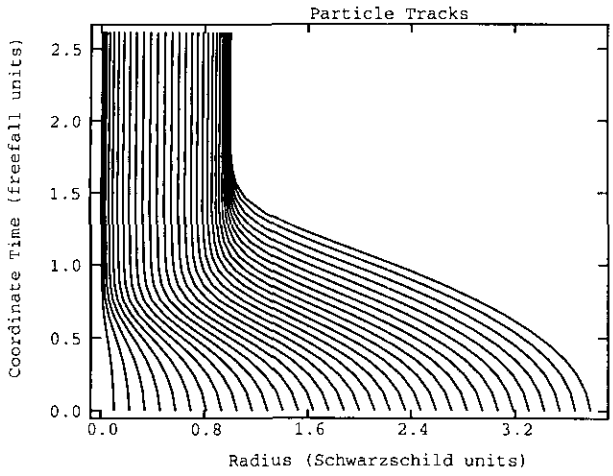

FIG. 3. Particle tracks for a 256-particle, 64-node pressureless collapse (59). Every eighth particle is plotted.

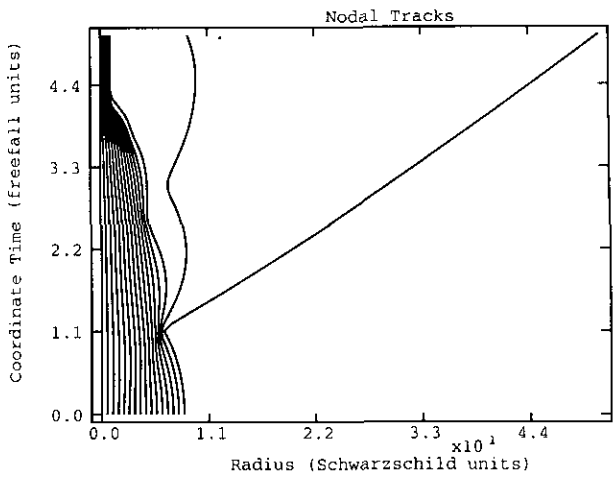

FIG. 5. Fluid tracks from the FEM code for the perturbed data of (60). There are 256 nodes and every 17th particle is plotted.

All such pressureless collapses are similar, and indeed both codes produce similar models. A typical run starts with the $w = 1.35$, $\gamma = \frac{5}{3}$ model of the static test and sets $\varepsilon = 0$. As with the Oppenheimer–Snyder solution there is freefall collapse to a black hole, with the evolution "stopping" as fluid elements reach their respective horizons. The overall characteristics are evident in Fig. 3, where some particles are tracked during their evolution.

The following parameters were used to make comparisons:

SPH	FEM
64 nodes	64 nodes
256 particles	
$\delta_c = 0.3$	$\delta_c = 0.3$
$K_{q1} = 1.0$	$K_{q1} = 0.5$
$K_{q2} = 1.0$	$K_{q2} = 0.5$

(59)

Note that a larger artificial viscosity is required for SPH.

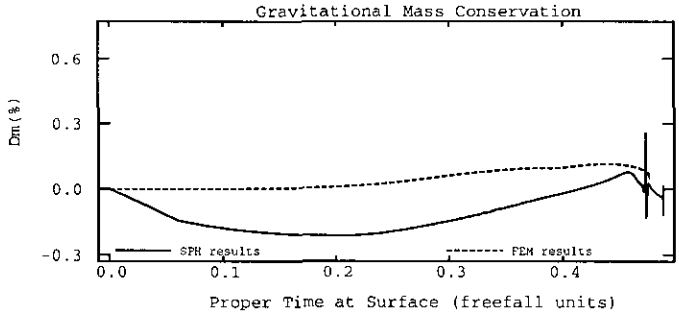

FIG. 4. Mass conservation for the collapse of Fig. 3. The FEM run crashes when the surface reaches its horizon (at $t \cong 0.47$) but the smoother SPH continues on with a small spike in the mass.

Surface oscillations in V can build up as the horizon is approached when smaller amounts are used. This is to be expected because the density and velocity are poorly approximated near the surface, where there are fewer particles.

There is excellent agreement between the two codes. The timescales are slightly different, with the FEM taking about 2% longer (proper time) for the surface to reach its Schwarzschild radius. A similar difference is evident in the lapse and central density.

As with the Oppenheimer–Snyder collapse the density spike (now at the centre) is smoothed out. Both methods show this behaviour, but the SPH spike is only about 20% of the FEM spike. The FEM, even though it uses fewer nodes (by a factor of four), has given a much better density spike.

The FEM conserves mass a bit better than SPH, but both

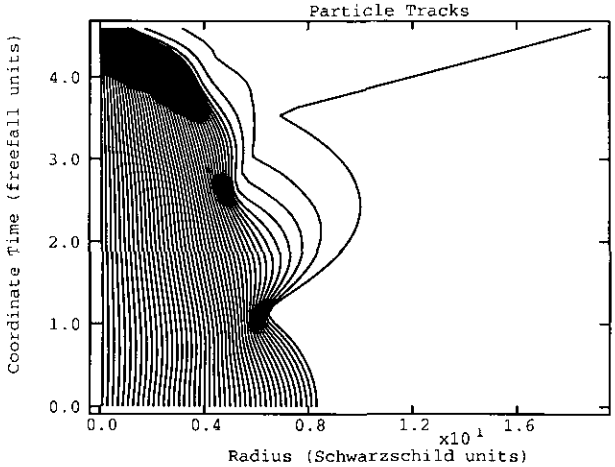

FIG. 6. Particle tracks from the SPH code for the perturbed data of (60). There are 256 particles and every sixth particle is plotted. This plot should be compared to the FEM results of Fig. 5.

are excellent (Fig. 4). Both codes were run until they crashed with $1 - 2m/r < 0$. The smoother SPH run successfully negotiates the final approach of the surface to its horizon, although a spike in mass conservation is evident at about $t = 0.47$ in Fig. 4. The FEM code crashes at this point.

Further tests used various perturbations of the internal energy. There are generally two types of behaviour: Hard equations of state, with γ above about $\frac{5}{3}$, give smooth (homologous) behaviours which are well modelled by both SPH and FEM, while softer equations of state result in bounces and shocks which are modelled up to the resolution inherent in the method.

These bounces almost invariably occur near the surface as shocks accelerate down the density slope. In these low density regions I would not expect SPH to perform accurately, but, in general, resolution seems to be the most important problem. A model which typifies these observations starts with a $\gamma = \frac{3}{2}$ polytrope and modifies the internal energy ε according to the formula

$$\varepsilon^{\text{new}} = \varepsilon^{\text{old}}(1 + \Delta\varepsilon(r)), \tag{60}$$

where $\Delta\varepsilon(r)$ is a cubic spline interpolation which takes the values 0.2 at the centre, 0 at 30% of the surface radius, and -0.4 at the surface. Therefore, the internal energy is increased near the centre and decreased near the surface.

The overall behaviour is given in Fig. 5 which shows the fluid tracks from an $n = 256$ node FEM run. The surface regions bounce violently off an expanding central core, and the surface then escapes at high velocity (about 50% of light speed). However, the material just within the surface reverses its outwards motion and again falls onto the core. Another, although softer, bounce occurs, and this material expands a bit and then falls back down. At this point the central regions have collapsed to form a black hole.

Note that this behaviour is extremely artificial. It arises from a peculiar choice of initial conditions and is not intended to reflect any particular physical evolution. It is an excellent test of the method,, however.

The extended outer envelope caused problems to the FEM, with negative densities appearing. An artificial viscosity of $K_{q1} = K_{q2} = 2$ was required to smooth out such low density perturbations.

An equivalent SPH run, with 256 particles, is illustrated by Fig. 6. The initial collapse and bounce is in agreement with SPH, but the bounce is much softer. The surface material does not immediately escape, but slows down and eventually collapses back onto the core. The *second* bounce is sufficiently strong to push the surface completely out. The interior regions are correctly collapsing to a black hole.

The surface position of the 256-particle SPH run is compared to a 64-node FEM run in Fig. 7. At this low FEM resolution the initial bounce is almost identical in both runs, with eventual recollapse and second bounce. The density near the surface is relatively small, but there are detail differences between SPH and FEM so the second bounce is only comparable in a qualitative sense.

The centre shows a difference in time scale (Fig. 8). The SPH produces a slower collapse (proper time) which again seems to reflect the extra smoothing inherent in the method.

Both SPH and FEM conserve mass well, with both runs showing a sudden increase when the black hole forms. This increase approached 5%, but it is probably due to the very few nodes (particles) which are left outside the horizon.

The bounces were rather smooth in both SPH and FEM. The FEM generally required about five nodes across the "shock," and there was no indication of oscillations before or behind the shock. The large viscosity could, however, result in drastic overestimates of the internal energy on the last two nodes as the zero-density problems mentioned previously were smoothed away.

The SPH shocks extended over about 20 particles, and with the smaller viscosity ($K_{q1} = K_{q2} = 1$) they developed oscillations just behind the shock as the shock reached the surface.

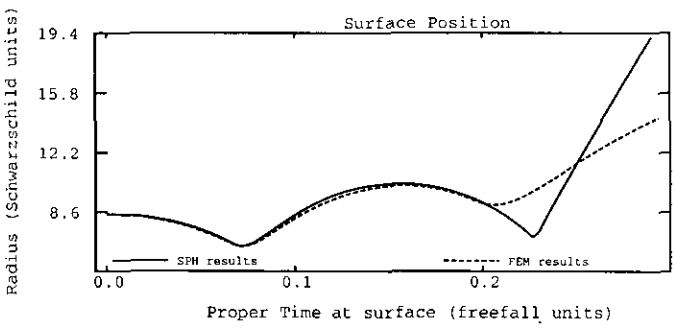

FIG. 7. Surface position for the evolutions of Fig. 5 and Fig. 6. The solid line is from the 256 particle run of Fig. 6, but the solid line is from a 64-node FEM run.

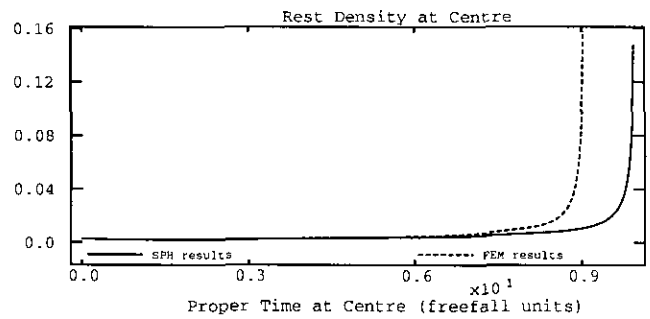

FIG. 8. Central rest density for the Fig. 6 SPH run (256 particles) compared to the Fig. 5 FEM run (256 nodes).

11. CONCLUSIONS

The modified SPH technique has successfully modelled fully relativistic collapse, albeit with the introduction of a grid for the evolution of metric quantities. The consistent use of density-weighted quantities S and E for the basic variables is important, as is the weighted residual approach which this consistency allows. These are necessary for the success of the method in spherical symmetry because of the coordinate problems. Coordinate problems are inherent to relativity so I expect that the use of a weighted residual method will always be necessary.

Kheyfets *et al.* [8] have extended SPH to relativity using a completely covariant approach which may alleviate these coordinate problems. This approach has not yet been applied to self-gravitating fluids.

In direct comparison with FEM the SPH has performed well in situations where there is high density and gravity is important. In regions where resolution is important, SPH is too smooth and can produce the anomalous results noted in the previous section. Experimentally it seems that SPH requires about four times as many particles as the FEM requires nodes. This number probably follows from the use of a kernel which extends over about four particles on either side. Smaller smoothing lengths resulted in poor shock tube simulations.

This factor of four also results in longer run times because more particles appear in the support of a particle basis function (kernel) than do nodes in the support of an FEM basis function. There is also some overhead imposed by the tests for neighbouring particles. However, for clarity and test purposes I have not included such algorithmic improvements as particle binning. Since there is no global gravitational particle–particle sum in my code (gravity is computed with the FEM grid), particle binning should result in computational times which increase linearly with the number of particles.

Note also that much of the three-dimensional nature of SPH is inherent in my code, while the FEM codes uses more specialized (to one dimension) constructs. Therefore relative efficiency is rather difficult to estimate.

The SPH may be naturally three-dimensional, but I must point out that the metric is very specifically spherical. Less symmetric metrics result in many more metric potentials, but more importantly, they give evolution equations and gravitational radiation. The FEM is, in theory, capable of handling such problems, but no attempts in this direction have yet been made.

I conclude that the SPH method has performed adequately in comparison with a completely FEM code. SPH has done well in the dense, gravitationally important central regions, but suffers from a lack of resolution when small scale fluid phenomena (shocks) are to be modelled. SPH is certainly able to cope with a self-gravitating, relativistic fluid and I would expect an improvement in performance if less symmetric situations are considered.

ACKNOWLEDGMENTS

The computer used for the development of these codes was supplied partly by a grant from the Natural Sciences and Engineering Research Council of Canada and partly by a grant from the Faculty of Science of the University of Western Ontario. I am grateful to Dr. T. Gaetz for many helpful discussions.

REFERENCES

1. A. J. Baker, *Finite Element Computational Fluid Mechanics* (Hemisphere, New York, 1983).
2. W. Benz, in *The Numerical Modelling of Nonlinear Stellar Pulsations*, edited by J. R. Buchler (Kluwer Academic, Amsterdam, 1990), p. 269.
3. J. Centrella and J. R. Wilson, *Astrophys. J. Supp.* **4**, 229 (1984).
4. M. R. Dubal, *Class. Quant. Gravity* **8**, 453 (1991).
5. A. E. Evrard, *Mon. R. Astron. Soc.* **235**, 911 (1988).
6. J. F. Hawley, L. L. Smarr, and J. R. Wilson, *Astrophys. J. Supp.* **55**, 211 (1984).
7. L. Hernquist and N. Katz, *Ap. J. Supp.* **70**, 419 (1989).
8. A. Kheyfets, W. A. Miller, and W. H. Zurek, *Phys. Rev. D* **41**, 451 (1990).
9. L. B. Lucy, *Astron. J.* **82**, 1013 (1977).
10. P. J. Mann, *Commun. Comput. Phys.* (1991).
11. P. J. Mann, *J. Comput. Phys.* **8**, 377 (1985).
12. C. W. Misner, K. S. Thorne, and J. A. Wheeler, *Gravitation* (Freeman, San Francisco, 1973).
13. J. J. Monaghan and R. A. Gingold, *J. Comput. Phys.* **52**, 374 (1983).
14. J. J. Monaghan and N. K. Lahy, in *Proceedings, Fifth Marcel Grossmann Meeting, 1988*, edited by D. G. Blair and M. J. Buckingham (World Scientific, Singapore, 1989), p. 1179.
15. J. J. Monaghan and J. C. Lattanzio, *Astron. Astrophys.* **149**, 135 (1985).
16. L. I. Petrich, S. L. Shapiro, and S. A. Teukolsky, *Phys. Rev. D* **33**, No. 8, 2100 (1986).
17. G. A. Sod, *J. Comput. Phys.* **7**, 1 (1978).
18. K. W. Thompson, *J. Fluid Mech.* **171**, 365 (1986).